

# Extended King integral for modeling of parametric array loudspeakers with axisymmetric profiles

Shao-Zhe Li,<sup>1</sup>  Tao Zhuang,<sup>1</sup>  Jia-Xin Zhong,<sup>2,a)</sup>  and Jing Lu<sup>1</sup> 

<sup>1</sup>Key Laboratory of Modern Acoustics and Institute of Acoustics, Nanjing University, Nanjing 210093, China

<sup>2</sup>Graduate Program in Acoustics, The Pennsylvania State University, University Park, Pennsylvania 16802, USA

## ABSTRACT:

Parametric array loudspeakers have been widely used in audio applications for generating directional audio beams. However, accurately calculating audio sound with a low computational load remains challenging, even for basic axisymmetric source profiles. This work addresses this challenge by extending the King integral in linear acoustics to incorporate both cumulative and local nonlinear effects, under the framework of the quasilinear solution without the paraxial approximation. The proposed method exploits the azimuthal symmetry in cylindrical coordinates to simplify modeling. To further improve computational efficacy, fast Hankel and Fourier transforms are employed for the radial and beam radiation directions, respectively. Numerical results with both uniform and focusing profiles demonstrate the advantages of the proposed approach over the traditional spherical wave expansion and direct integration methods, especially for larger aperture sizes. Specifically, for typical configurations with source aperture size of 0.2 m, we observe at least a 24-fold improvement in computational speed and a 227-fold reduction in memory requirements. These advancements allow us, for the first time, to present the sound field radiated by parametric array loudspeakers with a large aperture size of up to 0.5 m, without paraxial approximations. The implementation codes are available on [https://github.com/ShaoZhe-LI/PAL\\_King](https://github.com/ShaoZhe-LI/PAL_King). © 2024 Acoustical Society of America.

<https://doi.org/10.1121/10.0030403>

(Received 15 May 2024; revised 9 September 2024; accepted 13 September 2024; published online 7 October 2024)

[Editor: James F. Lynch]

Pages: 2189–2199

## I. INTRODUCTION

Parametric array loudspeakers (PALs) generate highly directional sound beams by leveraging the nonlinear effect of ultrasonic waves in the air.<sup>1</sup> This makes them widely applicable in various audio domains, such as active noise control,<sup>2,3</sup> material acoustic parameter measurement,<sup>4</sup> concealed weapon detection,<sup>5</sup> directional control,<sup>6</sup> and omnidirectional speaker construction.<sup>7</sup> Similar to the circular piston source in linear acoustics, the PAL with a uniform circular profile stands out as one of the most fundamental and widely used sources in various applications due to its straightforward design. Advanced beam manipulations, such as the steerable PAL, are commonly achieved using a phased array composed of circular elements,<sup>8</sup> primarily because most commercial ultrasonic transducers are manufactured in a circular shape. Moreover, the recently introduced focusing PAL,<sup>9</sup> designed to enhance the poor low-frequency response of conventional PALs, also adopts an axisymmetric yet focusing profile. Nevertheless, even for such straightforward cases of axisymmetric source profiles, accurately calculating the audio sound produced by PALs with high precision and low computational burden remains a significant challenge.

The direct integration method (DIM), which involves the direct evaluation of the quasilinear solution of the

Westervelt equation, is usually used to obtain the audio sound.<sup>10</sup> However, the computation is time-consuming because it contains the numerical evaluation of fivefold integrals, including twofold Rayleigh integrals over the area of the transducer surface to solve the ultrasonic field, and threefold integrals over the full space of the product of the source density and the Green's function for a point source to solve the audio sound field.<sup>11</sup> In addition, the Westervelt equation captures only the cumulative nonlinear effect. To include the local nonlinear effect, especially dominant in the near field where the wave field is complicated, the Kuznetsov equation is often employed.<sup>12</sup> This approach complicates calculations, because of the need to evaluate the Lagrangian density of the ultrasonic field.<sup>13</sup> As an alternative, the local effects can be incorporated without significant error by introducing an algebraic correction to the quasilinear solution derived from the Westervelt equation.<sup>14</sup> This method offers a reduction in computational complexity compared to the quasilinear solution of the Kuznetsov equation.

The well-known Khokhlov-Zabolotskaya-Kuznetsov (KZK) equation can be regarded as a paraxial approximation of the Westervelt equation,<sup>15</sup> and has been widely used to model the PAL.<sup>9</sup> To reduce the computation complexity, the Gaussian beam expansion (GBE) technique is commonly employed.<sup>16–18</sup> By expanding the source profile as a superposition of multiple Gaussian functions, the calculation is simplified, leveraging the analytical properties of Gaussian functions within the paraxial approximation. While the GBE

<sup>a)</sup>Email: Jiaxin.Zhong@psu.edu

technique notably reduces computational loads, the paraxial approximation can lead to inaccurate predictions, especially in the near field, regions distant from the axis, and at low audio frequencies. Recently, a steerable non-paraxial GBE was introduced to improve the prediction accuracy.<sup>19</sup> This approach utilized a non-paraxial approximation during the integration of virtual audio sources. This method facilitates more accurate calculations for field points located away from the axis and has subsequently been extended to model phased array PAL.<sup>20</sup> However, the non-paraxial approximation remains inaccurate for virtual audio source points situated away from the axis, leading to inaccuracies, particularly at small aperture sizes and low audio frequencies. Additionally, the paraxial approximation continues to be employed in calculating ultrasonic fields. Furthermore, Gaussian functions, not being a complete set, present constraints on the potential for further improving the prediction accuracy in GBE-based methods.<sup>21</sup>

Initially introduced in linear acoustics to address radiation from a baffled circular source,<sup>22,23</sup> the spherical wave expansion (SWE) offers an alternative approach for calculating the nonlinear sound fields generated by PALs. The key of the SWE approach is the representation of the Green's function in the spherical coordinate system, which streamlines the computation of both ultrasonic and audio fields by leveraging azimuthal symmetry. Within this framework, the angular component is characterized by spherical harmonics, while the radial component involves integrals with spherical Bessel functions. The SWE exhibits significantly faster convergence compared to the direct evaluation of the quasilinear solutions of the Westervelt and Kuznetsov equations,<sup>11,24</sup> all without the need for additional approximations. Furthermore, the SWE can be extended to model sphere scattering and the radiation of PALs with non-axisymmetric profiles.<sup>21,25</sup> However, it is worth noting that the computational demands of the SWE method increase with the source aperture size.

In linear acoustics, when computing radiation from a symmetric baffled circular source, one can transform the Rayleigh integral into the King integral by representing the Green's function in cylindrical coordinates.<sup>26,27</sup> Similar to the SWE, the calculation is simplified by exploiting the azimuthal symmetry without the need for additional approximations, while the incorporation of the fast Hankel transform (FHT) simplifies computations in the radial dimension, suggesting potential advantages over the SWE method.<sup>28,29</sup> This work extends the concept of the linear King integral to incorporate both cumulative and local nonlinear effects for calculating the audio sound generated by PALs with axisymmetric profiles. Furthermore, the FHT and fast Fourier transform (FFT) are implemented to improve the numerical computation speed in the transverse and beam radiation directions, respectively. Unlike the SWE method, the computational complexity of the proposed method is largely independent of aperture sizes, making it particularly advantageous for larger sizes. Simulation results for both uniform and focusing profiles, using typical aperture sizes,

are presented. Comparisons with the traditional SWE techniques demonstrate the efficacy of the proposed extended King integral method, particularly for large aperture sizes.

## II. THEORY

Figure 1 shows a baffled circular PAL with a radius of  $a$ . The  $z$ -axis is the radiation axis, while the source is located in the plane defined by the  $x$ -axis and  $y$ -axis. The field point location is denoted as  $\mathbf{r} = (x, y, z)$  or  $\mathbf{r} = (\rho, \varphi, z)$ , where  $(x, y, z)$  and  $(\rho, \varphi, z)$  are Cartesian and cylindrical coordinates, respectively. The source point on the transducer surface is denoted by  $\mathbf{r}_s = (x_s, y_s, z_s = 0) = (\rho_s, \varphi_s, z_s = 0)$ , and the virtual source point is represented by  $\mathbf{r}_v = (x_v, y_v, z_v) = (\rho_v, \varphi_v, z_v)$ .

When ultrasound beams at the frequencies of  $f_1$  and  $f_2$  ( $f_2 > f_1$ ) are emitted by the PAL, the audio sound at the frequency of  $f_a = f_2 - f_1$  is demodulated in air due to the second-order nonlinearity. For axisymmetric source profiles, the velocity boundary condition on the source surface is

$$v_{I,z}(\mathbf{r}_s, t) = v_0 [u_1(\rho_s) e^{-i\omega_1 t} + u_2(\rho_s) e^{-i\omega_2 t}], \quad (1)$$

where  $v_0$  is a velocity constant,  $\omega_i = 2\pi f_i$  is the angular frequency,  $t$  is the time,  $u_i(\rho_s)$  is the normalized excitation source profile at frequency  $f_i$ . Here, and in the sequel, the subscript  $i = 1, 2$  denotes the ultrasound index.

### A. Quasilinear solution of sound fields generated by a PAL under the cylindrical coordinate system

When local effects are neglected, the radiation of the PAL is governed by the well known Westervelt equation,<sup>10,12</sup> which, under the quasilinear approximation, can be decomposed into two coupled linear equations by using the method of successive approximations.<sup>24</sup> The audio field can be regarded as generated by the virtual sources, which are caused by the second-order nonlinear effects. The source density of these virtual sources is proportional to the product of ultrasound pressure and reads<sup>21</sup>

$$q(\mathbf{r}_v; \omega_a) = \frac{\beta \omega_a}{i \rho_0^2 c_0^4} p^*(\mathbf{r}_v; \omega_1) p(\mathbf{r}_v; \omega_2), \quad (2)$$

where  $\rho_0$  is the air density,  $c_0$  is the linear sound speed, and  $p(\mathbf{r}_v; \omega_i)$  represents the pressure at point  $\mathbf{r}_v$  at frequency  $f_i$ .

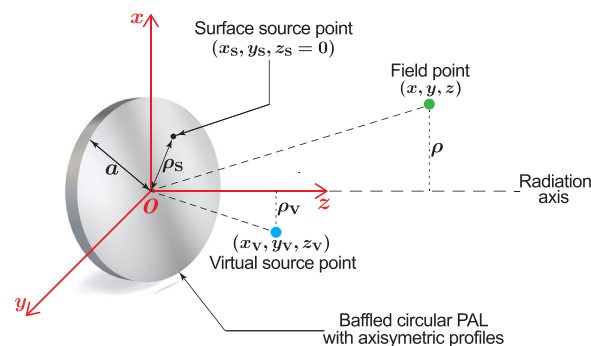


FIG. 1. (Color online) Sketch of a baffled circular PAL with axisymmetric profiles.

The asterisk denotes complex conjugate and the subscript “a” denotes the audio sound index.

The ultrasound pressure is usually solved by the Rayleigh integral,<sup>11</sup> which can be expressed in cylindrical coordinates as

$$p(\mathbf{r}; \omega_i) = -2i\rho_0 v_0 \omega_i \int_0^{2\pi} \int_0^\infty u(\rho_s) g(\mathbf{r}; \mathbf{r}_s; \omega_i) \rho_s d\rho_s d\varphi_s, \quad (3)$$

where  $g(\mathbf{r}; \mathbf{r}_s; \omega_i)$  is the Green’s function between the field point  $\mathbf{r}$  and the source point  $\mathbf{r}_s$  at frequency  $f_i$ , which is expressed as

$$g(\mathbf{r}; \mathbf{r}_s; \omega_i) = \frac{\exp(ik_i |\mathbf{r} - \mathbf{r}_s|)}{4\pi |\mathbf{r} - \mathbf{r}_s|}. \quad (4)$$

Here,  $k_i = \omega_i/c_0 + i\alpha(\omega_i)$  is the complex wavenumber,  $\alpha(\omega_i)$  is the attenuation coefficient at angular frequency  $\omega_i$ . The audio sound can be seen as the radiation from an infinitely large volume source with a density given by Eq. (2), and it is assumed that the vibrating piston radiating the primary wave is placed in an infinite baffle at the plane  $z = 0$ .<sup>16</sup> So that the audio sound pressure reads<sup>21</sup>

$$p(\mathbf{r}; \omega_a) = -i\rho_0 \omega_a \int_{-\infty}^{\infty} \int_0^{2\pi} \int_0^\infty q(\mathbf{r}_v; \omega_a) \times g(\mathbf{r}; \mathbf{r}_v; \omega_a) \rho_v d\rho_v d\varphi_v dz_v. \quad (5)$$

To include the local nonlinear effects, which the Westervelt equation can not capture, an algebraic correction to the quasilinear solution of the Westervelt equation has been proposed.<sup>14</sup> This correction is used in this work and the solution of the audio sound pressure becomes

$$\tilde{p}(\mathbf{r}; \omega_a) = p(\mathbf{r}, \omega_a) - \left[ \frac{\rho_0}{2} \mathbf{v}^*(\mathbf{r}; \omega_1) \cdot \mathbf{v}(\mathbf{r}; \omega_2) - \left( \frac{\omega_1}{\omega_2} + \frac{\omega_2}{\omega_1} - 1 \right) \frac{p^*(\mathbf{r}; \omega_1)p(\mathbf{r}; \omega_2)}{2\rho_0 c_0^2} \right], \quad (6)$$

where  $\mathbf{v}(\mathbf{r}; \omega_i) = \nabla p(\mathbf{r}; \omega_i)/(i\rho_0 \omega_i)$  is the particle velocity of ultrasound at frequency  $f_i$ .

## B. King integral for calculating ultrasound fields

The Green’s function given by Eq. (4) can be expanded as<sup>30</sup>

$$g(\mathbf{r}; \mathbf{r}_s; \omega_i) = \frac{i}{4\pi} \sum_{\nu=-\infty}^{\infty} \left[ \int_0^\infty \frac{\exp(i\sqrt{k_i^2 - k_\rho^2}|z - z_s|)}{\sqrt{k_i^2 - k_\rho^2}} \times J_\nu(k_\rho \rho_s) J_\nu(k_\rho \rho) k_\rho dk_\rho \right] e^{i\nu(\varphi - \varphi_s)}, \quad (7)$$

where  $J_\nu(\cdot)$  is the Bessel function of the first kind of order  $\nu$ . Substituting Eq. (7) into Eq. (3) and utilizing the

axisymmetry of the sound source velocity can yield the King integral,<sup>26</sup>

$$p(\mathbf{r}; \omega_i) = \rho_0 v_0 \omega_i \int_0^\infty \frac{\exp(i\sqrt{k_i^2 - k_\rho^2}|z|)}{\sqrt{k_i^2 - k_\rho^2}} \times \hat{u}(k_\rho) J_0(k_\rho \rho) k_\rho dk_\rho \\ = \rho_0 v_0 \omega_i \mathcal{H}_0^{-1} \left( \frac{\exp(i\sqrt{k_i^2 - k_\rho^2}|z|)}{\sqrt{k_i^2 - k_\rho^2}} \hat{u}(k_\rho) \right), \quad (8)$$

where the integrals with respect to  $\varphi_s$  are non-zero only when  $\nu = 0$ , and  $\hat{u}(k_\rho)$  is the zero-order Hankel transform of  $u(\rho_s)$  expressed as<sup>27</sup>

$$\hat{u}(k_\rho) = \int_0^\infty u(\rho_s) J_0(k_\rho \rho_s) \rho_s d\rho_s = \mathcal{H}_0(u(\rho_s)). \quad (9)$$

For convenience, the  $\nu$ -order Hankel transform pair for a function  $h(\rho)$  is introduced as<sup>31</sup>

$$\begin{cases} \hat{h}(k_\rho) = \mathcal{H}_\nu(h(\rho)) = \int_0^\infty h(\rho) J_\nu(k_\rho \rho) \rho d\rho, \\ h(\rho) = \mathcal{H}_\nu^{-1}(\hat{h}(k_\rho)) = \int_0^\infty \hat{h}(k_\rho) J_\nu(k_\rho \rho) k_\rho dk_\rho. \end{cases} \quad (10)$$

For convenience, we define

$$\hat{g}_0(k_\rho, z; \omega) \equiv \frac{i}{4\pi \sqrt{k^2 - k_\rho^2}} \exp(i\sqrt{k^2 - k_\rho^2}|z|) \\ = \mathcal{H}_0(g_0(\mathbf{r}; \mathbf{0}; \omega)), \quad (11)$$

where  $g_0(\mathbf{r}; \mathbf{0}; \omega)$  is the  $\nu = 0$  term of  $g(\mathbf{r}; \mathbf{0}; \omega)$ , and  $\hat{g}_0(k_\rho, z; \omega)$  can be seen as the zero-order Hankel transform of  $g_0(\mathbf{r}; \mathbf{0}; \omega)$  according to Eq. (7). Substituting Eq. (11) into Eq. (8) yields a more compact form of the King integral,

$$p(\mathbf{r}; \omega_i) = -4\pi i \rho_0 v_0 \omega_i \mathcal{H}_0^{-1}(\mathcal{H}_0(g_0(\mathbf{r}; \mathbf{0}; \omega_i)) \hat{u}(k_\rho)). \quad (12)$$

It is worth noting that while Eq. (11) provides an analytic form for  $\hat{g}_0(k_\rho, z; \omega)$ , the function is singular when  $k = k_\rho$ , which may lead to errors in numerical computations if directly utilizing the analytic formula in Eq. (11) to solve  $\hat{g}_0(k_\rho, z; \omega)$  in numerical calculations. Nevertheless,  $\hat{g}_0(k_\rho, z; \omega)$  can be also calculated as the Hankel transform of  $g_0(\mathbf{r}; \mathbf{0}; \omega_i)$  according to Eq. (11). However, there is no direct analytic expression for  $g_0(\mathbf{r}; \mathbf{0}; \omega_i)$ . Notably,  $g_0(\mathbf{r}; \mathbf{0}; \omega_i)$  represents the  $\nu = 0$  component of  $g(\mathbf{r}; \mathbf{0}; \omega)$ , while all other  $\nu \neq 0$  components of  $g(\mathbf{r}; \mathbf{0}; \omega)$  yield a null contribution to the integral in Eq. (3). Consequently, it is feasible to directly apply the Hankel transform to  $g(\mathbf{r}; \mathbf{0}; \omega)$  and engage in subsequent computational processes, that is,

$$p(\mathbf{r}; \omega_i) = -4\pi i \rho_0 v_0 \omega_i \mathcal{H}_0^{-1}(\mathcal{H}_0(g(\mathbf{r}; \mathbf{0}; \omega_i)) \hat{u}(k_\rho)). \quad (13)$$

Equation (13) is used for numerical calculation in this work.

In cylindrical coordinates, the particle velocity can be expressed as  $\mathbf{v}(\mathbf{r}; \omega_i) = \nabla p(\mathbf{r}, \omega_i) / (i\rho_0 \omega_i) = (v_\rho, v_\phi, v_z)$ , and by using Eqs. (8) and (13), its components are expressed as

$$\begin{cases} v_\rho(\mathbf{r}; \omega_i) = \frac{1}{i\rho_0 \omega_i} \frac{\partial p}{\partial \rho} \\ \quad = 4\pi v_0 \mathcal{H}_1^{-1}(k_\rho \mathcal{H}_0(g(\mathbf{r}; \mathbf{0}; \omega_i)) \hat{u}(k_\rho)), \\ v_\phi(\mathbf{r}; \omega_i) = 0, \\ v_z(\mathbf{r}; \omega_i) = \frac{1}{i\rho_0 \omega_i} \frac{\partial p}{\partial z} \\ \quad = v_0 \mathcal{H}_0^{-1}\left(\exp\left(i\sqrt{k_i^2 - k_\rho^2}|z|\right) \hat{u}(k_\rho)\right), \end{cases} \quad (14)$$

where the relation  $J'_0(x) = -J_1(x)$  is used. It is noted that the integrals in  $v_\rho(\mathbf{r}, \omega_i)$  and  $v_z(\mathbf{r}, \omega_i)$  are expressed in the form of the first order and zero-order Hankel transforms, respectively.

Equations (12) and (14) represent the (linear) King integrals used for calculating ultrasound pressure and particle velocity fields, respectively. For an axisymmetric source profile given by  $u(\rho_s)$ , its zero-order Hankel transform,  $\hat{u}(k_\rho)$  is calculated first using Eq. (9). Subsequently, the pressure and particle velocity fields can be obtained using Eqs. (12) and (14), respectively.

### C. Extended King integral for calculating audio sound fields

The conventional DIM for calculating audio fields involves numerical evaluations of fivefold integrals, which are rather time-consuming for numerical implementations.<sup>11</sup> In this subsection, we demonstrate that for axisymmetric source profiles, the King integral in linear acoustics can be extended to include nonlinearity enabling the calculation of the audio sound with simplified computational complexity.

Using the azimuthal symmetry of the source density  $q(\mathbf{r}_v; \omega_a)$  obtained by the ultrasound fields generated by the axisymmetric sound source, substituting Eq. (7) into Eq. (5), exchanging the integration order of  $k_\rho$  and  $\rho_v$  and utilizing the definition in Eq. (11), the audio sound pressure Eq. (5) can be simplified as

$$p(\mathbf{r}; \omega_a) = -2\pi i \rho_0 \omega_a \int_{-\infty}^{\infty} \int_0^{\infty} \hat{q}(k_\rho, z_v; \omega_a) \hat{g}_0(k_\rho, z - z_v; \omega_a) J_0(k_\rho) k_\rho dk_\rho dz_v. \quad (15)$$

Here, the zero-order Hankel transform of the source density function with respect to  $\rho_v$  is introduced as

$$\hat{q}(k_\rho, z_v; \omega_a) = \mathcal{H}_0(q(\mathbf{r}_v; \omega_a)). \quad (16)$$

After exchanging the integration order of  $k_\rho$  and  $z_v$  in Eq. (15), it is obtained that

$$p(\mathbf{r}; \omega_a) = \mathcal{H}_0^{-1}(\hat{p}(k_\rho, z; \omega_a)), \quad (17)$$

where we defined

$$\begin{aligned} \hat{p}(k_\rho, z; \omega_a) &= -2\pi i \rho_0 \omega_a \int_{-\infty}^{\infty} \hat{q}(k_\rho, z_v; \omega_a) \\ &\quad \hat{g}_0(k_\rho, z - z_v; \omega_a) dz_v. \end{aligned} \quad (18)$$

From Eq. (11), it is noted that  $\hat{g}_0(k_\rho, z - z_v; \omega_a)$  in Eq. (18) has a separable component of  $\exp\left(i\sqrt{k_a^2 - k_\rho^2}|z - z_v|\right)$ . Consequently, we introduce the Fourier transform pair,

$$\begin{cases} \hat{f}(k_z) = \mathcal{F}(\hat{f}(z)) = \int_{-\infty}^{\infty} \hat{f}(z) e^{-ik_z z} dz, \\ \hat{f}(z) = \mathcal{F}^{-1}(\hat{f}(k_z)) = \int_{-\infty}^{\infty} \hat{f}(k_z) e^{ik_z z} dk_z. \end{cases} \quad (19)$$

Define

$$\hat{q}(k_\rho, k_z; \omega_a) \equiv \mathcal{F}(\hat{q}(k_\rho, z; \omega_a)), \quad (20)$$

$$\hat{g}_0(k_\rho, k_z; \omega_a) \equiv \mathcal{F}(\hat{g}_0(k_\rho, z; \omega_a)), \quad (21)$$

then Eq. (18) can be expressed as

$$\hat{p}(k_\rho, z; \omega_a) = \mathcal{F}^{-1}(\hat{p}(k_\rho, k_z; \omega_a)), \quad (22)$$

where we defined

$$\hat{p}(k_\rho, k_z; \omega_a) = -2\pi i \rho_0 \omega_a \hat{q}(k_\rho, k_z; \omega_a) \hat{g}_0(k_\rho, k_z; \omega_a). \quad (23)$$

Similar to the equivalence of Eqs. (12) and (13),  $\hat{g}_0(k_\rho, z; \omega_a)$  in Eq. (23) is also replaced with  $\mathcal{H}_0(g(\mathbf{r}; \mathbf{0}; \omega_a))$  in numerical calculations to improve the accuracy. By substituting Eq. (22) into Eq. (17), the audio sound pressure has a final form of

$$p(\mathbf{r}; \omega_a) = \mathcal{H}_0^{-1}(\mathcal{F}^{-1}(\hat{p}(k_\rho, k_z; \omega_a))). \quad (24)$$

Equation (24) has a similar form of the King integral in linear acoustics [Eq. (12)]. Therefore, it is termed the *extended King integral* in this work.

In conclusion, the processes of how to obtain the audio fields generated by a PAL with axisymmetric profiles are as follows. First,  $\hat{g}_0(k_\rho, k_z; \omega_a)$  and  $\hat{q}(k_\rho, k_z; \omega_a)$  in Eq. (23), the spatial frequency domain of  $g_0(\mathbf{r}, \mathbf{0}, \omega_a)$  and  $q(\mathbf{r}_v; \omega_a)$ , respectively, are solved by using the Hankel and Fourier transforms, where  $\hat{g}_0(k_\rho, k_z; \omega_a)$  can be also replaced with the spatial frequency domain of  $g(\mathbf{r}, \mathbf{0}, \omega_a)$  shown in Eq. (4). Then, as shown in Eq. (24), the audio sound pressure  $p(\mathbf{r}; \omega_a)$  can be calculated through the inverse Hankel and Fourier transform of  $\hat{p}(k_\rho, k_z; \omega_a)$ , which is the product of  $\hat{g}_0(k_\rho, k_z; \omega_a)$  and  $\hat{q}(k_\rho, k_z; \omega_a)$ .

## III. NUMERICAL TECHNIQUES

### A. Fast Fourier transformation

The fast Fourier transform (FFT) is used for rapid computation of Fourier transforms involved in Eqs. (20), (21),

and (22). In numerical calculation,  $\hat{q}(k_\rho, z; \omega_a)$  and  $\hat{g}_0(k_\rho, z; \omega_a)$  are discretized with a spatial interval of  $\Delta_z$  in the  $z$ -direction. Then, Eq. (22) can be expressed as

$$\begin{aligned} \hat{p}[k_\rho, n; \omega_a] &= -2\pi i \rho_0 \omega_a \times \text{IFFT} [\text{FFT}(\hat{q}[k_\rho, n; \omega_a]) \\ &\quad \times \text{FFT}(\hat{g}_0[k_\rho, n; \omega_a])] \times \Delta_z, \end{aligned} \quad (25)$$

where FFT and IFFT represent the forward and inverse fast Fourier transforms, respectively.  $\hat{p}[k_\rho, n; \omega_a]$ ,  $\hat{q}[k_\rho, n; \omega_a]$  and  $\hat{g}_0[k_\rho, n; \omega_a]$  denote  $\hat{p}(k_\rho, z = n\Delta_z; \omega_a)$ ,  $\hat{q}(k_\rho, z = n\Delta_z; \omega_a)$  and  $\hat{g}_0(k_\rho, z = n\Delta_z; \omega_a)$ , respectively. The spatial domain in the  $z$ -direction is truncated to  $[-Z_u, Z_u]$ , which determines the range of the virtual audio source to be included. To mitigate aliasing in the range  $z \in (0, Z_u)$  caused by the truncation,  $\lfloor Z_u/\Delta_z \rfloor$  zeros are padded, as shown in Fig. 2. Here,  $Z_u$  represents the maximum distance in the  $z$ -direction of the audio sound field to be calculated.

## B. Fast Hankel transformation

The  $\nu$ -order Hankel transform pair is shown in Eq. (10), and the integrals in Eqs. (8), (9), (11)–(14), (16), (17), and (24) are all the form of (inverse) Hankel transform. The Hankel transform can be efficiently computed using the FFT, a method known as the FHT.<sup>28,29</sup> Its basic principle and implementation process are described as follows.

When numerically calculating Eq. (10), the integration range, which ideally extends infinitely, must be truncated. Define the truncation lengths as  $N_h$  and  $N_H$  for  $\rho$  and  $k_\rho$ , respectively. Let  $N_t = N_h \cdot N_H$ ,  $\rho = N_h \rho'$ , and  $k_\rho = N_H k'_\rho$ . Consequently, Eq. (10) can be modified to

$$\begin{cases} \tilde{H}(k'_\rho) = N_h^2 \int_0^1 \tilde{h}(\rho') J_\nu(N_t k'_\rho \rho') \rho' d\rho', \\ \tilde{h}(\rho') = N_H^2 \int_0^1 \tilde{H}(k'_\rho) J_\nu(N_t k'_\rho \rho') k'_\rho dk'_\rho, \end{cases} \quad (26)$$

where  $0 \leq \rho' \leq 1$ ,  $0 \leq k'_\rho \leq 1$ ,  $\tilde{h}(\rho') \equiv h(N_h \rho')$ ,  $\tilde{H}(k'_\rho) = \hat{h}(N_H k'_\rho)$ . Here,  $\tilde{h}$  and  $\tilde{H}$  represent the functions over the normalized domain  $[0, 1]$ . Both the forward and inverse Hankel transforms in Eq. (26) share a similar structure. The forward transform from  $\tilde{h}$  to  $\tilde{H}$  is denoted as  $\tilde{H} = \text{FHT}(\tilde{h}, N_h, N_H)$ , the inverse transform from  $\tilde{H}$  to  $\tilde{h}$  is expressed as  $\tilde{h} = \text{FHT}(\tilde{H}, N_H, N_h)$ .

Divide the interval  $[0, 1]$  into  $N$  subintervals using the  $N + 1$  points  $\xi_n$ , where  $0 = \xi_0 < \xi_1 < \dots < \xi_N = 1$ . The functions  $\tilde{h}(\rho')$  and  $\tilde{H}(k'_\rho)$  are sampled at  $N$  points  $\rho'_n$  and  $k'_{\rho,n}$  for  $n = 0, 1, 2, \dots, N - 1$ , respectively, such that

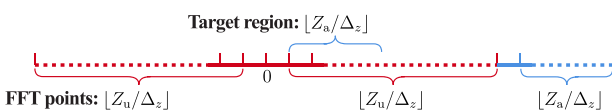


FIG. 2. (Color online) Sketch of the zero padding in the  $z$ -direction. The red line represents the number of sampling points of  $\hat{q}(k_\rho, z; \omega_a)$  and  $\hat{g}_0(k_\rho, z; \omega_a)$ , with a total of  $(2\lfloor Z_u/\Delta_z \rfloor + 1)$  points sampled, while the blue line represents the number of zeros padded, which are  $\lfloor Z_u/\Delta_z \rfloor$  in total.

$\xi_n \leq \rho'_n, k'_{\rho,n} \leq \xi_{n+1}$ . In numerical calculation,  $\tilde{h}(\rho')$  is approximated by  $\tilde{h}(\rho') \approx \tilde{h}(\rho'_n)$  for  $\xi_n \leq \rho' \leq \xi_{n+1}$ , and similarly for  $\tilde{H}(k'_\rho)$ . By utilizing  $\xi_0 = 0$  and  $\tilde{h}(\rho'_N) \equiv 0$ , and employing the relation  $\int_{\rho_1}^{\rho_2} \rho^\nu J_\nu(\rho) d\rho = \rho_2^\nu J_{\nu+1}(\rho_2) - \rho_1^\nu J_{\nu+1}(\rho_1)$ , Eq. (26) can be rewritten as

$$\begin{cases} \tilde{H}(k'_\rho) = \frac{N_h^2}{N_t k'_\rho} \sum_{n=0}^{N-1} \left[ \frac{\tilde{h}(\rho'_n)}{(\rho'_n)^\nu} - \frac{\tilde{h}(\rho'_{n+1})}{(\rho'_{n+1})^\nu} \right] \xi_{n+1}^{\nu+1} J_{\nu+1}(N_t k'_\rho \xi_{n+1}), \\ \tilde{h}(\rho') = \frac{N_H^2}{N_t \rho'} \sum_{n=0}^{N-1} \left[ \frac{\tilde{H}(k'_{\rho,n})}{(k'_{\rho,n})^\nu} - \frac{\tilde{H}(k'_{\rho,n+1})}{(k'_{\rho,n+1})^\nu} \right] \xi_{n+1}^{\nu+1} J_{\nu+1}(N_t \rho' \xi_{n+1}). \end{cases} \quad (27)$$

Define  $\xi_0 = 0$  and  $\xi_n = \exp[\tau(n - N)]$  for  $n = 1, 2, \dots, N$ , where  $\tau > 0$ . Here,  $\tau$  is determined by  $e^{\tau(1-N)} = 1 - e^{-\tau}$ . The sampling points of the functions  $\tilde{h}$  and  $\tilde{H}$  are set as  $\rho'_n = k'_{\rho,n} = \rho'_0 \exp(\tau n)$  for  $n = 0, 1, \dots, N - 1$ , with  $\rho'_0 = (1 + e^\tau)e^{-\tau N}/2$ . Based on these definitions, Eq. (27) is rewritten as

$$\begin{cases} \tilde{H}(k'_{\rho,m}) = \frac{N_h^2}{N_t k'_{\rho,m}} \sum_{n=0}^{N-1} \eta_h(n) j_{\nu+1}(n+m), \\ \quad m = 0, 1, 2, \dots, N-1, \\ \tilde{h}(\rho'_m) = \frac{N_H^2}{N_t \rho'_m} \sum_{n=0}^{N-1} \eta_H(n) j_{\nu+1}(n+m), \\ \quad m = 0, 1, 2, \dots, N-1, \end{cases} \quad (28)$$

where  $j_{\nu+1}(n) = J_{\nu+1}(N_t \rho'_0 \exp[\tau(n + 1 - N)])$  for  $n = 0, 1, 2, \dots, 2N - 1$ , and

$$\eta_h(n) = \begin{cases} \kappa_0 \left( \frac{\tilde{h}(\rho'_0)}{(\rho'_0)^\nu} - \frac{\tilde{h}(\rho'_1)}{(\rho'_1)^\nu} \right) \exp[(\nu + 1)\tau(1 - N)], \\ \quad n = 0, \\ \left( \frac{\tilde{h}(\rho'_n)}{(\rho'_n)^\nu} - \frac{\tilde{h}(\rho'_{n+1})}{(\rho'_{n+1})^\nu} \right) \exp[(\nu + 1)\tau(n + 1 - N)], \\ \quad n = 1, 2, \dots, N-1, \\ 0, \quad n = N, N+1, \dots, 2N-1, \end{cases}$$

with the coefficient  $\kappa_0 = (2e^\tau + e^{2\tau})/[(1 + e^\tau)^2(1 - e^{-2\tau})]$ . In Eq. (28),  $\eta_H(n)$  is defined similarly to  $\eta_h(n)$  by replacing  $\rho'_n$  and  $\tilde{h}(\rho'_n)$  with  $k'_{\rho,n}$  and  $\tilde{H}(k'_{\rho,n})$ , respectively. The summation in Eq. (28) can be seen as the cross correlation of  $\eta(n)$  and  $j_{\nu+1}(-n)$ , that is, the convolution of  $\eta(n)$  and  $j_{\nu+1}(-n)$ . Therefore, by using FFT and  $N_t = N_h N_H$ , Eq. (28) is rewritten as

$$\begin{cases} \tilde{H}(k'_{\rho,m}) = \text{FHT}(\tilde{h}, N_h, N_H) \\ \quad = \frac{N_h}{N_t k'_{\rho,m}} \text{FFT}\{\text{FFT}[\eta_h(n)] \times \text{IFFT}[j_{\nu+1}(n)]\}, \\ \tilde{h}(\rho'_m) = \text{FHT}(\tilde{H}, N_H, N_h) \\ \quad = \frac{N_H}{N_t \rho'_m} \text{FFT}\{\text{FFT}[\eta_H(n)] \times \text{IFFT}[j_{\nu+1}(n)]\}. \end{cases} \quad (29)$$

Equation (29) demonstrates that the proposed extended King integral can be efficiently computed in the  $\rho$ -direction using FFT.

#### IV. SIMULATION RESULTS

Numerical simulations are conducted on MATLAB R2023a. In this section, the parameters are set as follows if not specified. The sound speed  $c_0 = 343 \text{ m/s}$  and the air density  $\rho = 1.21 \text{ kg/m}^3$ . The coefficient of nonlinearity  $\beta = 1.2$ . The radius of the PAL is set as  $a = 0.1 \text{ m}$  in Sec. IV A and other values in Sec. IV A. The center frequency of the ultrasound is set as  $f_u = 40 \text{ kHz}$ . Consequently, the lower and upper ultrasound frequencies are  $f_1 = f_u - f_a/2$  and  $f_2 = f_u + f_a/2$ , respectively, where  $f_a$  is the audio frequency. The sound attenuation coefficient,  $\alpha_u$ , at 40 kHz is approximately  $0.15 \text{ Np/m}$  calculated according to ISO 9613-1 with a relative humidity of 70% and temperature of  $20^\circ\text{C}$ .<sup>32</sup> The validation and accuracy of the proposed method is examined in Sec. IV A for both uniform and focusing source profiles. The ultrasonic and audio field generated by PALs with large aperture sizes is presented in Sec. IV B. The advantage of the proposed method in computational efficacy over traditional methods is demonstrated in Sec. IV C.

##### A. Validation of the proposed method

###### 1. Uniform profile

Figure 3 illustrates the axial sound fields generated by a circular PAL with a uniform profile (piston source). Here, the source profile is  $u(\rho_s) = H(a - \rho_s)$ , where  $H(\cdot)$  is the Heaviside function. The ultrasound particle velocity in the  $\rho$ -direction is zero on the axis ( $\rho = 0$ ) due to the azimuthal symmetry. Therefore, it is not depicted in Fig. 3 for simplicity. The results on the axis cannot be calculated with the King integral-based approaches, due to the limitation of the sampling method employed in numerical implementation by utilizing FHT (see Sec. III B). Therefore, results at a line close to the radiation axis,  $\rho \approx 5.87 \times 10^{-4} \text{ m} \ll \lambda_u \approx 8.58 \times 10^{-3} \text{ m}$ , are used for comparison unless otherwise specified, where  $\lambda_u$  denotes the

wavelength of the ultrasound wave. The relative error, also presented in Fig. 3, is defined as

$$\epsilon_{\text{rel}} = \frac{|p_{\text{num}} - p_{\text{exact}}|}{|p_{\text{exact}}|}, \quad (30)$$

where  $p_{\text{num}}$  is the numerical calculation result obtained using the King integral-based approaches, and  $p_{\text{exact}}$  is the exact result calculated using Rayleigh integral and the DIM for ultrasound and audio sound fields, respectively. The relative error can be approximately expressed as

$$\epsilon_{\text{rel}} \approx \left| \frac{|p_{\text{num}}| - |p_{\text{exact}}|}{|p_{\text{exact}}|} \right| = \left| \left| \frac{p_{\text{num}}}{p_{\text{exact}}} \right| - 1 \right|, \quad (31)$$

so the difference in sound pressure level (SPL) calculated by the two methods is represented as

$$\begin{aligned} \Delta \text{SPL} &= |\text{SPL}_{\text{num}} - \text{SPL}_{\text{exact}}| \\ &= \left| 20 \log_{10} \left( \left| \frac{p_{\text{num}}}{p_{\text{exact}}} \right| \right) \right| \\ &= 20 \log_{10}(1 + \epsilon_{\text{rel}}), \end{aligned} \quad (32)$$

assuming that  $\epsilon_{\text{rel}} \ll 1$ . According to Eq. (32), a relative error of 1% corresponds to a SPL difference of approximately 0.086 dB.

As depicted in Figs. 3(d) and 3(e), at the same radial coordinate  $\rho = 5.87 \times 10^{-4} \text{ m}$ , the relative error between the ultrasound fields calculated by Rayleigh and King integrals is generally less than 1%, corresponding to an error of within 0.1 dB in SPL. This validates the accuracy of the numerical computation of the King integral. Although the relative error is larger when comparing the ultrasound fields at  $\rho = 5.87 \times 10^{-4} \text{ m}$  calculated using the King integral and those on the axis obtained using the Rayleigh integral, it still generally remains less than 10% and 1% for ultrasound pressure and particle velocity, respectively. Based on the accurate calculation of the ultrasound fields using the King integral, as shown in Fig. 3(f), the audio sound pressure obtained using the proposed extended King integral agrees

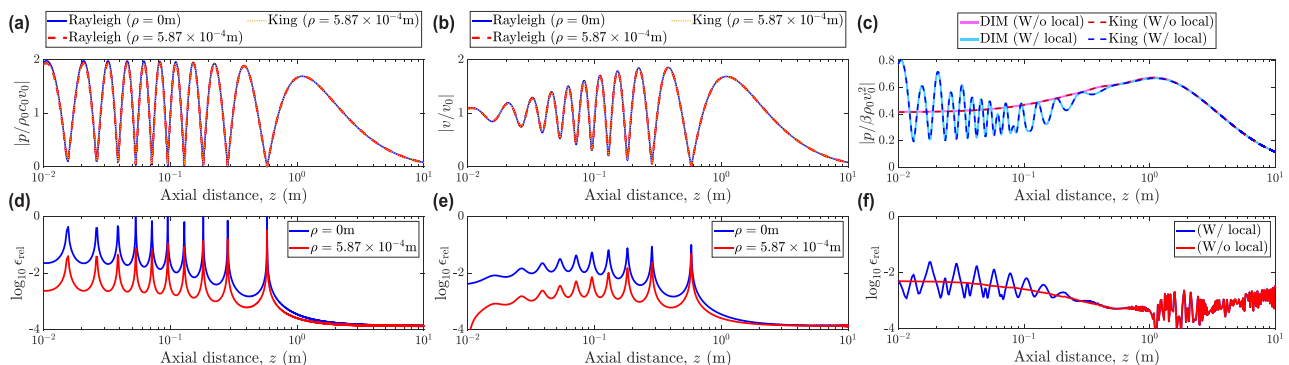


FIG. 3. (Color online) Axial ( $\rho = 0$ ) ultrasound (a), (d) pressure and (b), (e) particle velocity in the  $z$ -direction, and (c), (f) audio sound pressure generated by a PAL with a radius of  $a = 0.1 \text{ m}$  and a uniform profile. Ultrasound fields at 40 kHz are calculated by Rayleigh [Eq. (3)] and King [Eqs. (12) and (14)] integrals. Audio sound fields at 500 Hz are calculated using DIM [Eq. (5)] and the proposed extended King integral [Eq. (24)]. The legends ‘W/ local’ and ‘W/o local’ indicate whether the local nonlinearity is included or not, respectively. The bottom row shows the relative error defined by Eq. (30).

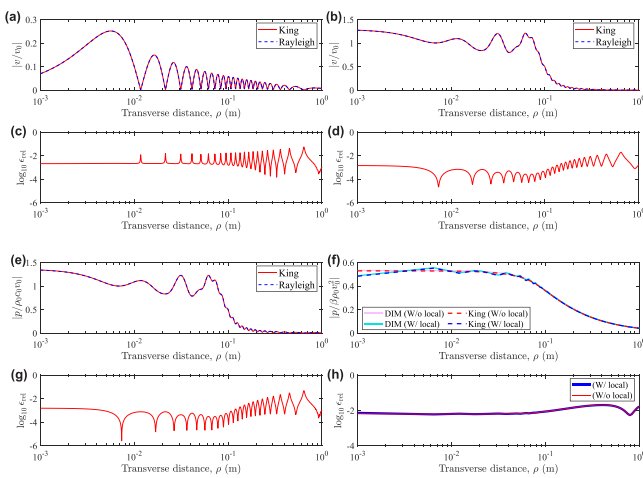


FIG. 4. (Color online) Transverse ultrasound particle velocity in (a), (c)  $\rho$ - and (b), (d)  $z$ -directions, and transverse (e), (g) ultrasound and (f), (h) audio sound pressure at  $z = 0.2$  m generated by a PAL with a radius of  $a = 0.1$  m and a uniform profile. The ultrasound and audio sound frequencies are 40 kHz and 500 Hz, respectively. (c), (d), (g), and (h) show the relative error for (a), (b), (e), and (f).

well with that obtained using the conventional DIM, showcasing a general relative error of less than 1%.

The transverse sound fields generated by a circular PAL with a uniform profile at two typical  $z$  coordinates are presented in Fig. 4 ( $z = 0.2$  m) and Fig. 5 ( $z = 1$  m). According to Figs. 4(c), 4(d), 4(g), 5(c), 5(d), and 5(g), the relative error between the ultrasound fields calculated by Rayleigh and King integrals generally remains below 1% (less than 0.1 dB in SPL), dropping to less than 0.1% (less than 0.01 dB in SPL) near the axis in Figs. 4(d), 4(g), 5(d), and 5(g). This further validates the accuracy of numerically computing the King integral using the FHT determining the sound field at transverse field points. Similar to Fig. 3(f), the results presented in Figs. 4(h) and 5(h) illustrate the

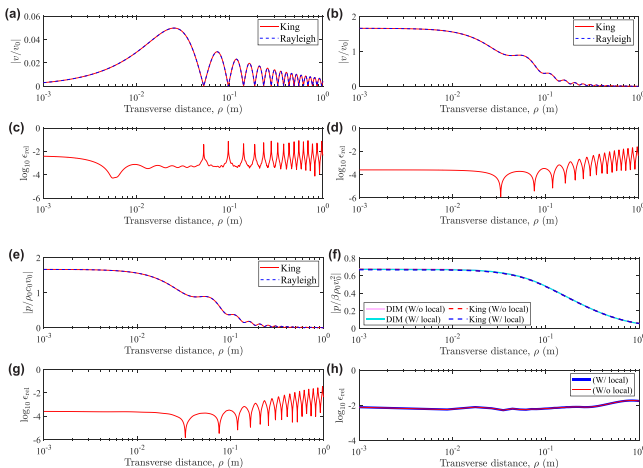


FIG. 5. (Color online) Transverse ultrasound particle velocity in (a), (c)  $\rho$ - and (b), (d)  $z$ -directions, and transverse (e), (g) ultrasound and (f), (h) audio sound pressure at  $z = 1$  m generated by a PAL with a radius of  $a = 0.1$  m and a uniform profile. The ultrasound and audio sound frequencies are 40 kHz and 500 Hz, respectively. Figures (c), (d), (g), (h) show the relative error for (a), (b), (e), and (f).

negligible relative error (generally less than 1%) when calculating the transverse audio sound pressure using the proposed extended King integral.

## 2. Focusing profile

Another important application featuring axisymmetric profiles is the use of focusing PALs.<sup>9</sup> Similar to the sound fields generated by a circular PAL with a uniform profile (shown in Figs. 3, 4, and 5), the axial and transverse sound fields at  $z = 0.2$  m and  $z = 1$  m generated by a circular PAL with a focusing profile are illustrated in Figs. 6, 7, and 8 in this section, respectively, where the focal length is set as  $F = 0.2$  m. Here, the source profile is  $u_i(\rho_s) = \exp(-i\sqrt{\rho_s^2 + F^2}\omega_i/c_0)$ . As depicted in Figs. 6(d)-6(f), 7(c), 7(d), 7(g), 7(h), and 8(c), 8(d), 8(g), and 8(h), the relative error between the King and Rayleigh integrals, and the proposed extended King integral and the conventional DIM, is also generally less than 1%, which is equivalent to less than 0.1 dB in SPL.

## B. PALs with large aperture sizes

The proposed extended King integral method offers a significant advantage: its computational complexity is generally unaffected by the size of the source aperture, thanks to the mechanism of the FHT. Consequently, the proposed method is especially advantageous for modeling circular PALs with large aperture sizes, a task that poses challenges for conventional approaches.<sup>12,24</sup> In this section, we present, for the first time, the two-dimensional (2D) sound field radiated by a circular PAL with large aperture sizes (up to 0.5 m) using the proposed method. This presentation is made without relying on the paraxial approximations typically assumed in conventional Gaussian beam expansions.<sup>16,19,33</sup> It is noted that, apart from the radius, all other parameters are set as described in Sec. IV. The audio sound fields with and without local effects differ only near the piston and are almost the same in the far field. Therefore, for the sake of brevity, only the results with local effects are shown in this section.

### 1. Uniform profile

The audio sound fields generated by a PAL with a uniform profile at several typical aperture sizes (from 0.05 to 0.5 m) are presented in Fig. 9 at 500 Hz. It is observed that the directional audio beam becomes progressively wider at larger aperture sizes. Additionally, it is worth noting that in Fig. 9, a low sound pressure area appears near the source surface, and its dimension increases as the radius increases.

Figure 10 presents the audio fields generated by uniform PALs with a radius of  $a = 0.5$  m. However, the audio sound frequencies are 500 Hz, 1 kHz, 2 kHz, and 4 kHz, corresponding to the audio sound wavelengths 68.6, 34.3, 17.15, and 8.58 cm, respectively. It is observed in Fig. 10 that, when the radius is large compared to the audio sound wavelength, the sound pressure shows noticeable troughs and peaks near the source surface. The number of peaks and troughs increases as the audio frequency increases.

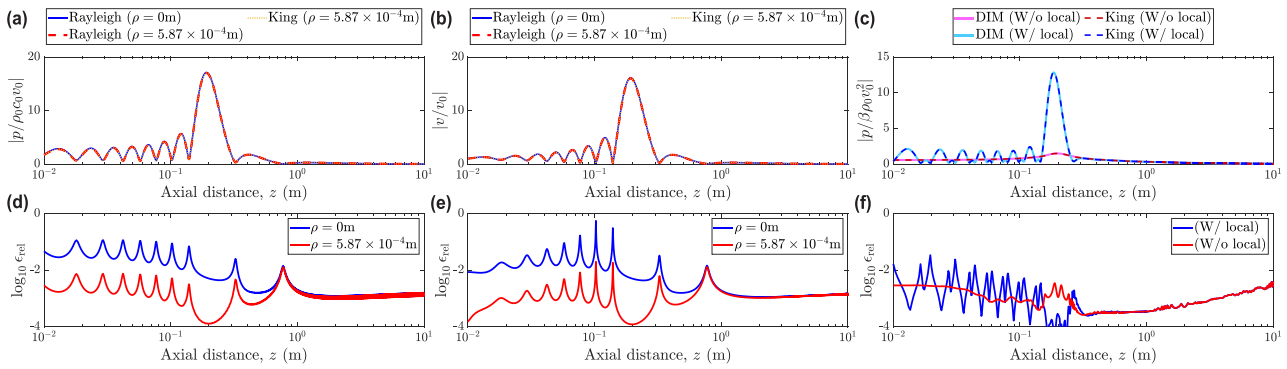


FIG. 6. (Color online) Axial ( $\rho = 0$ ) ultrasound (a), (d) pressure and (b), (e) particle velocity in  $z$  direction, and (c), (f) audio sound pressure generated by a PAL with a radius of  $a = 0.1$  m and a focal length of 0.2 m. The ultrasound and audio sound frequencies are 40 kHz and 500 Hz, respectively. The bottom row shows the relative error defined by Eq. (30).

Specifically, the number is approximately proportional to the ratio of the radius of the PAL to the wavelength of the audio sound. The proposed extended King integral method enables us to understand the audio beam behavior of conventional PALs at large aperture sizes.

## 2. Focusing profile

The audio sound fields generated by a focusing PAL with a focal length of 0.2 m are presented in Fig. 11 at different radii. Because the sound pressure amplitude in the area near the focal point is much larger than that in other areas, it is enlarged in a subfigure to show the details. It is observed that the audio beams become more focused near the focal point as the aperture size increases. This suggests that the poor low-frequency response of conventional PALs can be further improved by increasing the source size.<sup>9</sup> It is noted that in Fig. 11(a), the beam focusing near the focal point is not observed due to the diffraction limit of

ultrasound waves. Here, the critical distance for ultrasound, obtained using  $a^2/\lambda_u$ , is only 0.29 m.

Figure 12 presents the audio fields generated by a focusing PAL with a radius of  $a = 0.5$  m at different audio sound frequencies. It is observed that the acoustic contrast between the sound pressure near the focal point and other areas decreases as the audio frequency increases. This behavior can be attributed to the fact that the cumulative nonlinearity dominates the audio sound pressure field at higher audio frequencies, while the local nonlinearity generally remains independent of the audio frequency. It is this local nonlinearity that predominantly contributes to the beam focusing,<sup>9</sup> which is also illustrated in Fig. 6(c). At 4 kHz as shown in Fig. 12, sidelobes are even observed, lowering the contrast performance at the focal point. This indicates that the focusing performance is more apparent at low audio frequencies when the aperture size is large. The extended King integral method proposed in this work offers a convenient tool to analyze the specific effects of physical parameters such as aperture size and audio frequency on focusing PALs.

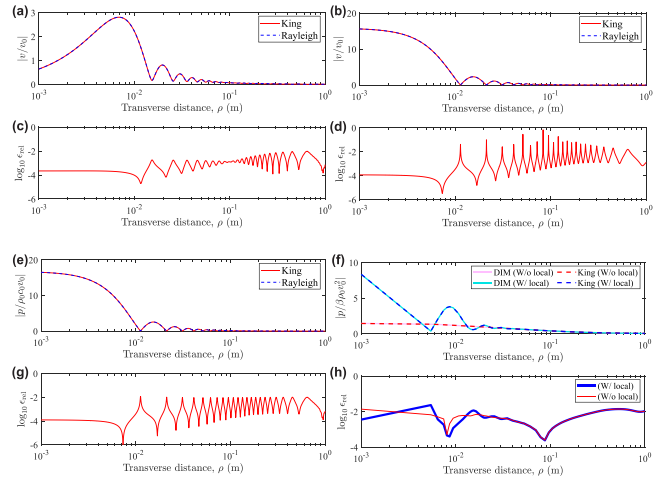


FIG. 7. (Color online) Transverse ultrasound particle velocity in (a), (c)  $\rho$ - and (b), (d)  $z$ -directions, and transverse (e), (g) ultrasound and (f), (h) audio sound pressure at  $z = 0.2$  m generated by a PAL with a radius of  $a = 0.1$  m and a focal length of 0.2 m. The ultrasound and audio sound frequencies are 40 kHz and 500 Hz, respectively. (c), (d), (g), and (h) show the relative error for (a), (b), (e), and (f).

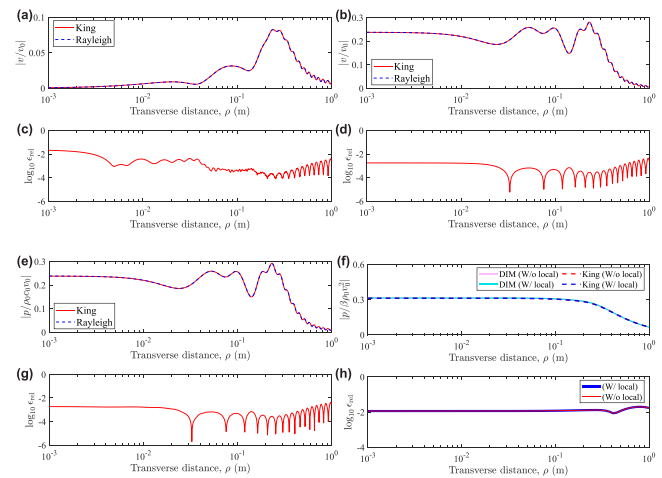


FIG. 8. (Color online) Transverse ultrasound particle velocity in (a), (c)  $\rho$ - and (b), (d)  $z$ -directions, and transverse (e), (g) ultrasound and (f), (h) audio sound pressure at  $z = 1$  m generated by a PAL with a radius of  $a = 0.1$  m and a focal length of 0.2 m. The ultrasound and audio sound frequencies are 40 kHz and 500 Hz, respectively. (c), (d), (g), and (h) show the relative error for (a), (b), (e), and (f).

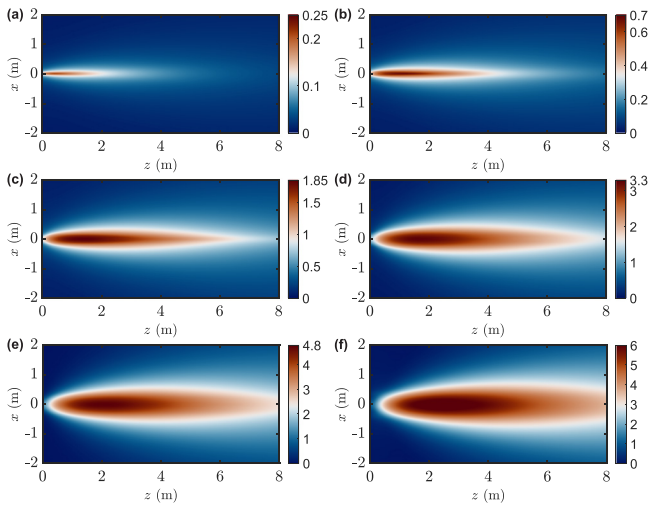


FIG. 9. (Color online) The 2D audio sound fields at  $y = 0$  plane generated by a circular PAL with a uniform profile and a radius of (a)  $a = 0.05$  m, (b)  $a = 0.1$  m, (c)  $a = 0.2$  m, (d)  $a = 0.3$  m, (e)  $a = 0.4$  m, and (f)  $a = 0.5$  m. The audio sound frequency is 500 Hz, and the normalized sound pressure amplitude,  $|p/\beta\rho_0v_0^2|$ , is plotted.

### C. Computational efficacy

The proposed extended King integral method offers a significant advantage in terms of low computing time and memory usage. For instance, in the DIM, the computational complexity is  $\mathcal{O}(N^2)$  for  $N$  points in each spatial dimension, resulting in a total complexity of  $\mathcal{O}(N^4)$  in two dimensions. In contrast, the computational complexity of our proposed approach is determined by the FFT and FHT in the  $z$ - and  $\rho$ -directions, respectively. The implementation of the FHT involves three FFT operations, as shown in Eq. (30), placing its computational complexity on par with that of FFT. Consequently, our method inherently has a computational complexity of  $\mathcal{O}(N \log N)$  in each spatial dimension. To demonstrate this advantage, we compared the computational efficiency of the proposed extended King integral method with that of the conventional DIM, which directly evaluates Eq. (5). In addition, we include the SWE method for comparison, as it is capable of calculating sound fields generated by circular

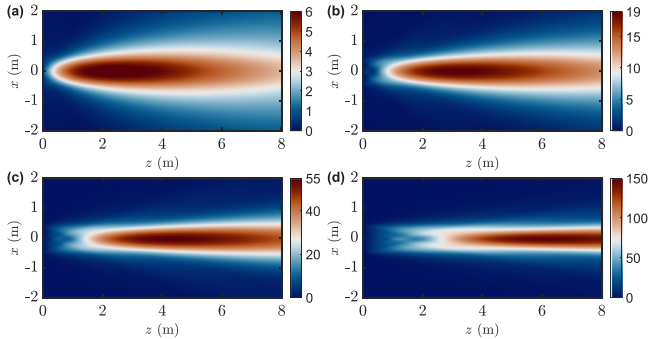


FIG. 10. (Color online) The 2D audio sound fields at  $y = 0$  plane generated by a circular PAL with a uniform profile and a radius of  $a = 0.5$  m. The audio sound frequencies (wavelengths) are (a) 500 Hz (68.6 cm), (b) 1 kHz (34.3 cm), (c) 2 kHz (17.15 cm), and (d) 4 kHz (8.58 cm), and the normalized sound pressure amplitude,  $|p/\beta\rho_0v_0^2|$ , is plotted.

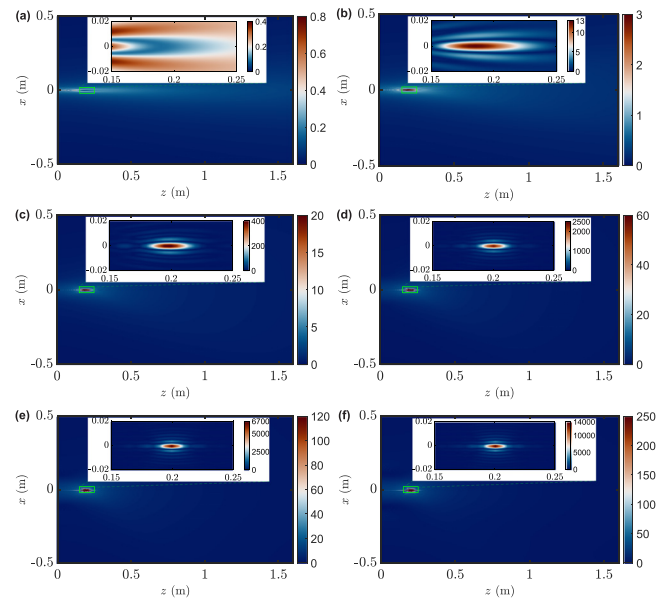


FIG. 11. (Color online) The 2D audio sound fields at  $y = 0$  plane generated by a circular PAL with a focal length of 0.2 m and a radius of (a)  $a = 0.05$  m, (b)  $a = 0.1$  m, (c)  $a = 0.2$  m, (d)  $a = 0.3$  m, (e)  $a = 0.4$  m, and (f)  $a = 0.5$  m, and the normalized sound pressure amplitude,  $|p/\beta\rho_0v_0^2|$ , is plotted.

PALs with axisymmetric profiles.<sup>9,11,24</sup> In this subsection, the numerical results are obtained using a computer equipped with an Intel(R) Xeon(R) Silver 4116 central processing unit (CPU) with 1 TB of random access memory (RAM). Figure 13 compares the computing time and memory usage of the proposed extended King integral, as well as the SWE and DIM methods, at different radii. These computations were performed to obtain a 2D sound field at the  $y = 0$  plane, similar to those shown in Figs. 9–12, where the range extends from 0 to 1.5 m in the  $\rho$ -direction and from 0 to 3 m in the  $z$ -direction.

When calculating the ultrasound and audio sound field with the extended King integral, the maximum value in the  $\rho$ -direction is set as  $\rho_{\max} = 2$  m and the number of sampling points is set as  $N = 16\,384$ . Our FFT-based method is actually

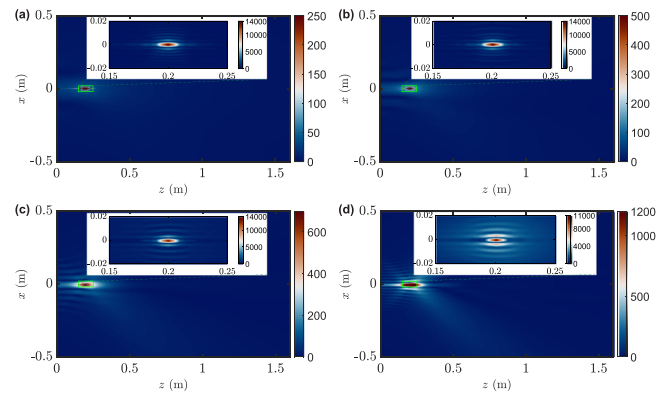


FIG. 12. (Color online) The 2D audio sound fields at  $y = 0$  plane generated by a circular PAL with a focal length of 0.2 m and a radius of  $a = 0.5$  m. The audio sound frequencies (wavelengths) are (a) 500 Hz (68.6 cm), (b) 1 kHz (34.3 cm), (c) 2 kHz (17.15 cm), and (d) 4 kHz (8.58 cm). The normalized sound pressure amplitude,  $|p/\beta\rho_0v_0^2|$ , is plotted.

quite similar to the angular spectrum method used in linear acoustics.<sup>34–39</sup> Previous studies have discussed the convergence of the method when the sampling interval is less than half the wavelength.<sup>34,35</sup> The only difference between our method and the angular spectrum method is that we also use FFT to compute the integration for the audio sound in the  $z$ -direction. Therefore, in the  $z$ -direction, the discrete interval is set as  $\Delta_z = \lambda_2/2$ . Specifically,  $[Z_u/\Delta_z] = 4224$  for calculating the ultrasound field with  $Z_u = 18$  m. Similarly,  $[Z_a/\Delta_z] = 704$  for calculating the audio sound field with  $Z_a = 3$  m. Consequently, the total number of samples in the  $z$ -direction is given by  $2[Z_u/\Delta_z] + [Z_a/\Delta_z] + 1 = 9153$ , as illustrated in Fig. 2. Here,  $\lambda_2$  represents the wavelength of the upper ultrasound at  $f_2 = 40.25$  kHz. In this case, the error between the results of the proposed method and those by the SWE and DIM methods is generally less than 0.1 dB. For the SWE calculations, the sound field is discretized into 6000 points, with 100 points in the radial direction and 60 in the zenithal direction, under the spherical coordinate system. When implementing the DIM in MATLAB to calculate sound fields, matrix operations are used to expedite the computation. The Gauss-Legendre quadrature is used for numerical integration. Specifically, we first segment the integration region and then perform integration within each segment. The length of each segment is set to  $(3/2)\lambda_u$ , where  $\lambda_u$  is the ultrasonic wavelength. Within each segment, we employ a three-point Gauss-Legendre quadrature method. However, due to the limited

computer memory (1 TB), only 30 field points can be calculated at a time. Consequently, the total computing time required by the DIM to calculate sound fields at 6000 points can be estimated to be 200 times the computing time needed to calculate results at 30 points.

Figure 13 illustrates that the computing time and memory usage of the proposed extended King integral method remains nearly constant at different radii. This is because the computational complexity of the FHT and FFT is almost independent of the radius, as demonstrated in the numerical computation process described in Sec. III. In contrast, the computing time and memory usage of the SWE method approximate quadratic functions with the radius. As a result, SWE requires significant computational resources, especially at larger aperture sizes. For example, at a radius of 0.01 m, the time and memory usage of SWE is even smaller than that of the proposed extended King integral. However, when the radius increases to 0.2 m, the computing time and memory usage of SWE increase to 24 and 227 times larger, respectively, compared to the proposed extended King integral. Additionally, the computational resources required by the DIM are much higher than those of the other two methods. For instance, at a radius of 0.01 m, the computing time and required memory of the DIM are approximately 94 and four times larger than those of the proposed method, respectively.

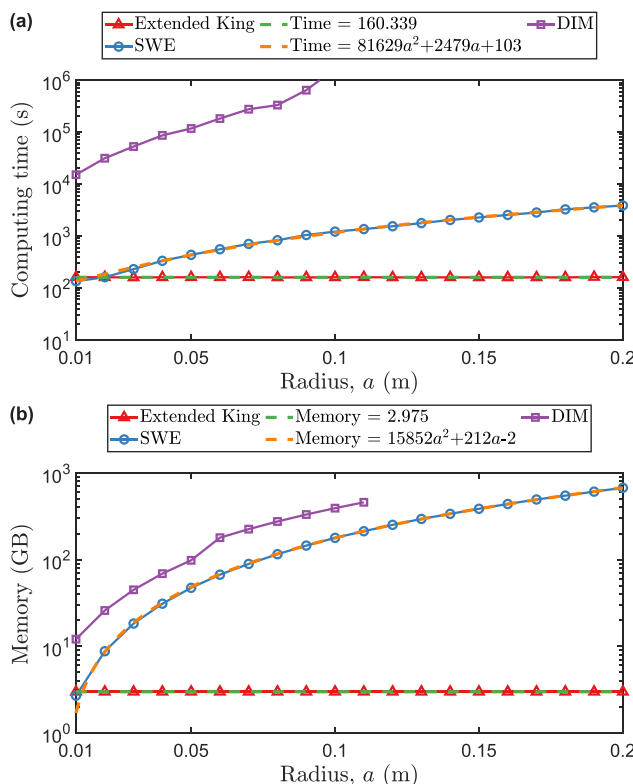


FIG. 13. (Color online) The computing (a) time and (b) memory required by the proposed extended King integral, DIM, and SWE method at different source radii.

## ACKNOWLEDGMENTS

This work was supported by the National Natural Science Foundation of China (Grant No. 12274221).

## AUTHOR DECLARATIONS

### Conflict of Interest

The authors have no conflicts of interest to disclose.

## DATA AVAILABILITY

Partial data and MATLAB codes are available at [https://github.com/ShaoZhe-LI/PAL\\_King](https://github.com/ShaoZhe-LI/PAL_King). Additional data supporting the findings of this study are available from the corresponding author upon reasonable request.

- <sup>1</sup>W.-S. Gan, J. Yang, and T. Kamakura, "A review of parametric acoustic array in air," *Appl. Acoust.* **73**(12), 1211–1219 (2012).
- <sup>2</sup>K. Tanaka, C. Shi, and Y. Kajikawa, "Binaural active noise control using parametric array loudspeakers," *Appl. Acoust.* **116**, 170–176 (2017).
- <sup>3</sup>J. Zhong, T. Zhuang, R. Kirby, M. Karimi, H. Zou, and X. Qiu, "Quiet zone generation in an acoustic free field using multiple parametric array loudspeakers," *J. Acoust. Soc. Am.* **151**(2), 1235–1245 (2022).
- <sup>4</sup>B. Castagnéde, A. Moussatov, D. Lafarge, and M. Saeid, "Low frequency in situ metrology of absorption and dispersion of sound absorbing porous materials based on high power ultrasonic non-linearly demodulated waves," *Appl. Acoust.* **69**(7), 634–648 (2008).
- <sup>5</sup>K. Rudd and M. Hinders, "Simulation of incident nonlinear sound beam and 3D scattering from complex targets," *J. Comput. Acoust.* **16**(03), 427–445 (2008).
- <sup>6</sup>W.-S. Gan and C. Shi, "Grating lobe elimination in steerable parametric loudspeaker," *IEEE Trans. Ultrason. Ferroelectr. Freq. Control.* **58**(2), 437–450 (2011).
- <sup>7</sup>U. Sayin, P. Artís, and O. Guasch, "Realization of an omnidirectional source of sound using parametric loudspeakers," *J. Acoust. Soc. Am.* **134**(3), 1899–1907 (2013).
- <sup>8</sup>C. Shi, "Investigation of the steerable parametric loudspeaker based on phased array techniques," Ph.D. thesis, Nanyang Technological University, Nanyang, China, 2013.
- <sup>9</sup>J. Zhong, T. Zhuang, R. Kirby, M. Karimi, X. Qiu, H. Zou, and J. Lu, "Low frequency audio sound field generated by a focusing parametric array loudspeaker," *IEEE/ACM Trans. Audio. Speech. Lang. Process.* **30**, 3098–3109 (2022).
- <sup>10</sup>P. J. Westervelt, "Parametric acoustic array," *J. Acoust. Soc. Am.* **35**(4), 535–537 (1963).
- <sup>11</sup>J. Zhong, R. Kirby, and X. Qiu, "A spherical expansion for audio sounds generated by a circular parametric array loudspeaker," *J. Acoust. Soc. Am.* **147**(5), 3502–3510 (2020).
- <sup>12</sup>M. Červenka and M. Bednářík, "A versatile computational approach for the numerical modelling of parametric acoustic array," *J. Acoust. Soc. Am.* **146**(4), 2163–2169 (2019).
- <sup>13</sup>S. I. Aanonsen, T. Barkve, J. N. Tjøtta, and S. Tjøtta, "Distortion and harmonic generation in the nearfield of a finite amplitude sound beam," *J. Acoust. Soc. Am.* **75**(3), 749–768 (1984).
- <sup>14</sup>M. Červenka and M. Bednářík, "An algebraic correction for the Westervelt equation to account for the local nonlinear effects in parametric acoustic array," *J. Acoust. Soc. Am.* **151**(6), 4046–4052 (2022).
- <sup>15</sup>M. F. Hamilton and D. T. Blackstock, *Nonlinear Acoustics* (Academic Press, San Diego, CA, 1998), Vol. 237.
- <sup>16</sup>M. Červenka and M. Bednářík, "Non-paraxial model for a parametric acoustic array," *J. Acoust. Soc. Am.* **134**(2), 933–938 (2013).
- <sup>17</sup>J. J. Wen and M. A. Breazeale, "A diffraction beam field expressed as the superposition of Gaussian beams," *J. Acoust. Soc. Am.* **83**(5), 1752–1756 (1988).
- <sup>18</sup>J. Yang, K. Sha, W.-S. Gan, and J. Tian, "Modeling of finite-amplitude sound beams: Second order fields generated by a parametric loudspeaker," *IEEE Trans. Ultrason. Ferroelectr. Freq. Control.* **52**(4), 610–618 (2005).
- <sup>19</sup>T. Zhuang, J. Zhong, F. Niu, M. Karimi, R. Kirby, and J. Lu, "A steerable non-paraxial Gaussian beam expansion for a steerable parametric array loudspeaker," *J. Acoust. Soc. Am.* **153**(1), 124–136 (2023).
- <sup>20</sup>Y. Zhu, W. Ma, Z. Kuang, M. Wu, and J. Yang, "Optimal audio beam pattern synthesis for an enhanced parametric array loudspeaker," *J. Acoust. Soc. Am.* **154**(5), 3210–3222 (2023).
- <sup>21</sup>J. Zhong, R. Kirby, M. Karimi, and H. Zou, "A spherical wave expansion for a steerable parametric array loudspeaker using Zernike polynomials," *J. Acoust. Soc. Am.* **152**(4), 2296–2308 (2022).
- <sup>22</sup>T. Douglas Mast and F. Yu, "Simplified expansions for radiation from a baffled circular piston," *J. Acoust. Soc. Am.* **118**(6), 3457–3464 (2005).
- <sup>23</sup>M. A. Poletti, "Spherical expansions of sound radiation from resilient and rigid disks with reduced error," *J. Acoust. Soc. Am.* **144**(3), 1180–1189 (2018).
- <sup>24</sup>J. Zhong, R. Kirby, and X. Qiu, "The near field, Westervelt far field, and inverse-law far field of the audio sound generated by parametric array loudspeakers," *J. Acoust. Soc. Am.* **149**(3), 1524–1535 (2021).
- <sup>25</sup>J. Zhong, R. Kirby, M. Karimi, H. Zou, and X. Qiu, "Scattering by a rigid sphere of audio sound generated by a parametric array loudspeaker," *J. Acoust. Soc. Am.* **151**(3), 1615–1626 (2022).
- <sup>26</sup>L. V. King, "On the acoustic radiation field of the piezo-electric oscillator and the effect of viscosity on transmission," *Can. J. Res.* **11**(2), 135–155 (1934).
- <sup>27</sup>M. Greenspan, "Piston radiator: Some extensions of the theory," *J. Acoust. Soc. Am.* **65**(3), 608–621 (1979).
- <sup>28</sup>V. Magni, G. Cerullo, and S. De Silvestri, "High-accuracy fast Hankel transform for optical beam propagation," *J. Opt. Soc. Am. A* **9**(11), 2031–2033 (1992).
- <sup>29</sup>D. Zhang, X.-C. Yuan, N. Ngo, and P. Shum, "Fast Hankel transform and its application for studying the propagation of cylindrical electromagnetic fields," *Opt. Express* **10**(12), 521–525 (2002).
- <sup>30</sup>J. Cheng, *The Principle of Acoustics* (Science Press, Beijing, 2019), pp. 208–209.
- <sup>31</sup>H. Johnson, "An improved method for computing a discrete Hankel transform," *Comput. Phys. Commun.* **43**(2), 181–202 (1987).
- <sup>32</sup>ISO 9613-1:1993, "Acoustics—Attenuation of sound during propagation outdoors—Part 1: Calculation of the absorption of sound by the atmosphere" (International Organization for Standardization, Geneva, Switzerland, 1993).
- <sup>33</sup>P. Ji, E.-L. Tan, W.-S. Gan, and J. Yang, "A comparative analysis of preprocessing methods for the parametric loudspeaker based on the Khokhlov–Zabolotskaya–Kuznetsov equation for speech reproduction," *IEEE Trans. Audio. Speech. Lang. Process.* **19**(4), 937–946 (2011).
- <sup>34</sup>D. P. Orobino and P. C. Pedersen, "Efficient angular spectrum decomposition of acoustic sources. i. theory," *IEEE Trans. Ultrason. Ferroelectr. Freq. Control.* **40**(3), 238–249 (1993).
- <sup>35</sup>P. Wu, R. Kazys, and T. Stepinski, "Optimal selection of parameters for the angular spectrum approach to numerically evaluate acoustic fields," *J. Acoust. Soc. Am.* **101**(1), 125–134 (1997).
- <sup>36</sup>X. Zeng and R. J. McGough, "Evaluation of the angular spectrum approach for simulations of near-field pressures," *J. Acoust. Soc. Am.* **123**(1), 68–76 (2008).
- <sup>37</sup>J. Blackmore, R. O. Cleveland, and J. Mobley, "Spatial filters suppress ripple artifacts in the computation of acoustic fields with the angular spectrum method," *J. Acoust. Soc. Am.* **144**(5), 2947–2951 (2018).
- <sup>38</sup>P. Wu, R. Kazys, and T. Stepinski, "Analysis of the numerically implemented angular spectrum approach based on the evaluation of two-dimensional acoustic fields. Part I. Errors due to the discrete Fourier transform and discretization," *J. Acoust. Soc. Am.* **99**(3), 1339–1348 (1996).
- <sup>39</sup>E. G. Williams and J. D. Maynard, "Numerical evaluation of the rayleigh integral for planar radiators using the FFT," *J. Acoust. Soc. Am.* **72**(6), 2020–2030 (1982).